Seismogenic Inversion Layer: Depth-dependent Slow Earthquakes Controlled by Temperature Dependence of Brittle-ductile Transitional Rheology

Ryosuke Ando[1], Kohtaro Ujiie[2], Naoki Nishiyama[3], and Yasushi Mori[4]

[1]University of Tokyo
[2]University of Tsukuba, Japan
[3]Geological Survey of Japan, National Institute of Advanced Industrial Science and Technology
[4]Kitakyushu Museum of Natural History and Human History

November 24, 2022

Abstract

The discovery of slow earthquakes illuminates the existence of a strange depth dependence of seismogenesis, which contradicts the common understanding of smooth brittle/seismic-ductile/aseismic transition as going deeper into the Earth's surface layers. However, within the transitional layer on plate interfaces, observations have clarified slip velocities of slow earthquakes changing from those slower to faster with increasing depth, as described by the "seismogenic inversion layer." We propose a new mechanical model that can consistently explain the classic brittle-ductile transition and this inversion phenomenon by considering the heterogeneous fault zone composed of brittle blocks in the ductile matrix. The key mechanism is the interplay between the volumetric fraction of brittle blocks and the viscosity of the surrounding plastically deformed matrix, where the former and the latter decrease with increasing temperature. This model is extended to shallow-slow earthquakes. Our results open a new pathway to infer the deformation mechanisms underlying slow earthquakes.

Hosted file

`grl220921supmat.docx` available at https://authorea.com/users/523867/articles/604946-seismogenic-inversion-layer-depth-dependent-slow-earthquakes-controlled-by-temperature-dependence-of-brittle-ductile-transitional-rheology

Title

Seismogenic Inversion Layer: Depth-dependent Slow Earthquakes Controlled by Temperature Dependence of Brittle-ductile Transitional Rheology

Authors

Ryosuke Ando,[1]* Kohtaro Ujiie,[2] Naoki Nishiyama,[3] Yasushi Mori[4]

Affiliations

[1] Graduate School of Science, University of Tokyo, Tokyo, Japan.

[2] Graduate School of Science and Technology, University of Tsukuba, Tsukuba, Japan

[3] Geological Survey of Japan, National Institute of Advanced Industrial Science and Technology, Tsukuba, Japan

[4] Kitakyushu Museum of Natural History and Human History, Kitakyushu, Japan

Corresponding author: Ryosuke Ando (ando@eps.s.u-tokyo.ac.jp)

Key Points:

- Depth-dependence of slow earthquakes is characterized as the seismogenic inversion layer (SIL); not monotonic brittle-ductile transition
- A simple and general physics-based model is proposed to describe the depth dependence of slow earthquakes with particular attention to SIL
- The key mechanism is the reduction of both the fraction of brittle blocks and viscosity of plastically deformed matrix in fault zones

Abstract

The discovery of slow earthquakes illuminates the existence of a strange depth dependence of seismogenesis, which contradicts the common understanding of smooth brittle/seismic-ductile/aseismic transition as going deeper into the earth's surface layers. However, within the transitional layer on plate interfaces, observations have clarified slip velocities of slow earthquakes changing from those slower to faster with increasing depth, as described by the "seismogenic inversion layer." We propose a new mechanical model that can consistently explain the classic brittle-ductile transition and this inversion phenomenon by considering the heterogeneous fault zone composed of brittle blocks in the ductile matrix. The key mechanism is the interplay between the volumetric fraction of brittle blocks and the viscosity of the surrounding plastically deformed matrix, where the former and the latter decrease with increasing temperature. This model is extended to shallow-slow earthquakes. Our results open a new pathway to infer the deformation mechanisms underlying slow earthquakes.

Plain Language Summary

We have believed that the earth's surface is cold and crispy while the interior is warm and soft, and the crispy layer called the seismogenic layer gradually changes to the soft layer, not generating earthquakes, with going deeper into the earth along plate interfaces. However, recent observations show that this change is not actually gradual. Instead, it involves the layer of the reverse tendency that we call the "Seismogenic Inversion Layer (SIL)" that hosts so-called deep slow earthquakes. To explain this enigmatic phenomenon, we propose a simple mechanical model based on the fundamental laws of rock physics. We find the key mechanism that generates SIL is the change in the rock property depending on the temperature inside the earth. Given rocks are composed of relatively crispy parts and soft parts, SIL is explained only if we consider the crispy parts shrink and the soft parts become softer with increasing temperature and depth.

1. Introduction

The depth dependence of the slow earthquakes has become established with some localities [*Frank et al.*, 2015; *Obara*, 2011; *Shelly and Johnson*, 2011; *Wech et al.*, 2009], but the underlying mechanism is poorly understood. Figure 1a and Table 1 summarize the observed depth-dependent features, presenting significantly different modes of slow earthquakes. Below the regular seismogenic depth, the modes of slow earthquakes are changed from long-term slow slip events (L-SSEs), short-term SSEs (S-SSEs) and tremors [*Obara*, 2011; *Wech et al.*, 2009]. We call them deep-slow earthquakes that occur

65 down-dip of the seismogenic zone, contrasted with shallow-slow earthquakes up-dip of
66 the seismogenic zone. The L-SSEs are much slower and larger slip or stress release events
67 in the durations of months to years [*Miyazaki et al.*, 2006] with less seismic
68 radiation[*Frank et al.*, 2015] than S-SSEs in the durations of weeks to a month [*Hirose*
69 *and Obara*, 2005; *Rogers and Dragert*, 2003]. Interestingly, L-SSEs are typically found
70 in the Nankai (Japan) [*Kobayashi*, 2017] and Guerrero (Mexico) [*Frank et al.*, 2015]
71 subduction zones. While L-SSEs are yet to be found in the transform fault such as the San
72 Andreas fault (USA) and the Cascadia (USA/Canada) subduction zone, the slip there may
73 be more steady in the corresponding depth range[*Michel et al.*, 2019]. Below the depth of
74 L-SSEs and after-slips [*Shelly and Johnson*, 2011], the area of S-SSEs exists as
75 overlapped with the tremor area [*Obara*, 2011], as often called episodic tremor and slip
76 (ETS). Further, detailed observations show that the peak of the slip amount is located at
77 a shallower depth than that of the tremor generation during an ETS episode [*Wech et al.*,
78 2009].

79 These observations illuminate the existence of the enigmatic depth range, which
80 is characterized by the peak of the slip speed within the transition zone, as schematically
81 illustrated in Figure 1a. This depth range may be called "the seismogenic inversion layer
82 (SIL)." As noted previously [*Scholz*, 1998], the existence of this peak at the intermediate
83 depth contradicts our expectation from the monotonic transition of the frictional
84 instability from the seismogenic (velocity-weakening) shallow layer to the aseismic
85 (velocity strengthening) deep layers, as often described by the negative to the positive
86 transition of the $(a - b)$ value invoking the rate- and state-dependent friction [*Liu and*
87 *Rice*, 2007; *Tse and Rice*, 1986] (Figure 1b). Available physics-based models for slow
88 earthquakes [*Ando et al.*, 2012; *Liu and Rice*, 2007; *Matsuzawa et al.*, 2013; *Segall et al.*,
89 2010; *Skarbek et al.*, 2012] are yet to identify the intrinsic mechanism of the depth-
90 dependent slow earthquake modes or the origin of SIL. Qualitative geological models,
91 attributing the slab dehydration [*Hyndman et al.*, 2015] and the mantle-wedge structure
92 [*Katayama et al.*, 2012], are limited to specific subduction zone conditions.

93 Notably, the abovementioned characterization appears to be applicable as
94 independent of tectonic settings, whether a transform fault [*Shelly and Johnson*, 2011;
95 *Wech et al.*, 2012], or the subduction interfaces [*Obara*, 2011; *Wech et al.*, 2009]. The
96 conditions of fault zone materials would be different in these plate interfaces, as
97 summarized in Supplementary Table 1. Petrological studies suggest that slow earthquakes
98 are independent of specific metamorphic reactions, considered the presumed higher
99 temperature range in Cascadia than Nankai [*Peacock*, 2009]. The depth-dependent
100 features have been interpreted regarding the material discontinuity with Moho [*Obara*,

101 2011] and the subduction dehydration and fluid migration [*Hyndman et al.*, 2015].
102 However, the above observations show the universal depth-dependence; this motivates us
103 to explore a more general primary control rather than those specific to the tectonic settings,
104 mineral compositions and metamorphisms.

105 This study seeks the primary controlling factor of the depth-dependent slow
106 earthquakes by focusing on the most basic rheological property of subduction-related
107 mélange shear zones: the dependence on the ambient temperature. Well examined are
108 the positive temperature dependences of the frictional velocity-dependence $(a - b)$
109 [*Blanpied et al.*, 1995; *Scholz*, 2019] and the negative dependence of the viscosity of
110 the rock plasticity [*Karato*, 2008], respectively (Figure 1b). However, their properties in
111 the transition zone have no consensus, while geological examples suggest the
112 importance of the mixed brittle and ductile components [*Burgmann*, 2018; *Fagereng et*
113 *al.*, 2014]. To unify the geological and geophysical observations, we construct and
114 analyze a physics-based model with the rheological heterogeneity of brittle patches in
115 the ductile matrix [*Ando et al.*, 2012]. The key ingredient of our model is the
116 temperature effect on the rock viscosity and the brittle over ductile fraction in the
117 mélange shear zones (Figure 1c).

118

2 Modeling and analysis method

  2.1 Geological observation

121 We begin by developing our geological picture of mélange shear zones at the
122 brittle-ductile transition depths. Figure 2a shows an example of a block-in-matrix
123 structure that is developed in the Nishikashiyama mélange deformed at the pressure of
124 ~1.0 GPa and the temperature of ~500 ºC under epidote-amphibolite facies metamorphic
125 condition [*Mori et al.*, 2014; *Tulley et al.*, 2022; *Ujiie et al.*, 2022]. The Nishikashiyama
126 mélange is marked by competent blocks of metabasite and metapelite in the chlorite-
127 actinolite schist (CAS) matrix that is considered to originate from mechanical mixing and
128 chemical reactions between serpentinite and metabasite near the mantle wedge corner
129 [*Mori et al.*, 2014; *Nishiyama*, 1989; 1990]. The matrix foliation is defined by the
130 alignment of chlorite and actinolite, commonly showing asymmetric fabrics such as S-C
131 fabric with their shear sense consistent with megathrust shear (Figure 2a) [*Tulley et al.*,
132 2022; *Ujiie et al.*, 2022]. The recent quartz grain-size piezometry and quartz flow law
133 analyses indicated the CAS matrix recorded an increase in strain rate of ~10^{-10} s^{-1}, which
134 may be comparable to slow slip strain rates [*Ujiie et al.*, 2022]. The stability field of
135 chlorite and actinolite [*Hacker et al.*, 2003] (Figure 2b) suggests that the assemblage of
136 chlorite-actinolite is likely ubiquitous along plate interfaces, including the P-T range of

137 the ETS zones [*Peacock*, 2009]. We presume that the observed block-in-matrix structure
138 in the Nishikashiyama mélange represents heterogeneous shear zones at source regions
139 of ETS (Figure 1c). Such heterogeneity was also reported not only from the subduction
140 zone setting [*Behr et al.*, 2018; *Fagereng et al.*, 2014; *Ujiie et al.*, 2018] but also from the
141 crustal/transform fault setting [*Scholz*, 2019; *Sibson*, 1977]. There, the brittle (or yield)-
142 strength can emerge from stress chains supported by the blocks (Figure 2c, top), and the
143 ductile strength becomes effective due to the matrix flow once the stress chains collapse
144 during slip events (Figure 2c, bottom), as in granular experiments [*Boyer et al.*, 2011;
145 *Howell et al.*, 1999].

146

147 **2.2 Mechanical model**

148 We next develop a new mechanical model to consider the macroscopic fault
149 motion obeying the concerned brittle-ductile mixed property (Figure 1c). As illustrated
150 in Figure 3a, we take a standard approach to simply model the average movement of the
151 finite fault area in a "macroscopic" viewpoint [*Bos and Spiers*, 2002; *Daub et al.*, 2011;
152 *Scholz*, 1998]: the one degree-of-freedom system with the parallel connection of the
153 spring-slider and the dashpot (Figure 3b) to incorporate the mixture of brittle (light grey)
154 and ductile (dark grey) fault zone rheology as previously done [*Daub et al.*, 2011]. Here,
155 we introduce the parameter called the brittle fraction R_b to describe "microscopic"
156 characteristics on the fault as the fraction of the area occupied by the brittle patches over
157 a fault area; R_b plays a major role to describe the temperature dependence as described in
158 the following section. Our model describes the fault strength solely by the frictional slider
159 at the brittle limit ($R_b = 1$) and by the dashpot at the ductile limit ($R_b = 0$), and by both
160 within the transitional regime ($0 < R_b < 1$). The equation of motion (EoM) for this
161 model is described by $m\ddot{u}(t) = -k\{u(t) + V_{pl}t + f\{\dot{u}(t)\}$ with the rheological strength

162
$$f(\dot{u}) = \begin{cases} f_s(R_b) & if\ \dot{u} = 0\ (stick) & (1a) \\ \alpha(R_b)|\dot{u}|^{1/n} + f_d(R_b) & if\ \dot{u} \neq 0\ (slip), & (2b) \end{cases}$$

163 where $u(t)$ denotes the displacement at time t with the dot denoting the temporal
164 derivative, m the mass, k the spring constant, V_{pl} the tectonic loading rate. The ductile
165 strength is characterized by α (velocity-strengthening ratio) and the constants n (stress
166 exponent). The brittle strength is simply described by the static friction f_s and the sliding
167 friction f_d $(< f_s)$, and we ignore the secondary transition process from f_s to f_d.
168 Additionally, while we simplify the model by the fully rigid block, the case when the
169 block deforms ductilely is discussed in Supplementary discussion B.

170

171 **2.3 Time-dependent solution**

172   Before detailing the temperature dependence, for a demonstration purpose, the
173 EoM is analytically solved assuming $n = 1$ and $V_{pl} = 0$ with the initial condition $\dot{u}(0) = 0$
174 0 and $u(0) = f_s/k$, which corresponds to a slip event occurring when the tectonic load
175 attained the static frictional strength f_s. The particular solution for the slip (the
176 displacement of the spring) is given by the well-known dumped oscillator solution:
177    $u(t) = \exp(-\gamma\omega t)\{(1 + \gamma/\xi)\exp(\omega\xi t) + (1 - \gamma/\xi)\exp(-\omega\xi t)\}(f_s - f_d)/(2k)$
178 with $\gamma = \alpha/(2\sqrt{mk})$, $\xi = \sqrt{\gamma^2 - 1}$ and $\omega = \sqrt{k/m}$. As plotted in Figure 3c, the solution
179 varies with the damping coefficient γ from the oscillatory if $0 < \gamma < 1$ (under damping),
180 monotonic if $\gamma \geq 1$ (over damping), to the non-inertia limit if $\gamma \gg 1$. Because slow
181 earthquakes are closer to the non-inertia (aseismic) regime, hereafter, we examine the
182 solution for $\gamma \gg 1$, reduced to
183        $u(t) = (\max u)\exp(-kt/\alpha)$ with $\max u = (f_s - f_d)/k$
184 and
185        $\dot{u}(t) = (\max \dot{u})\exp(-kt/\alpha)$ with $\max \dot{u} = (f_s - f_d)/\alpha$.
186 Besides, the non-Newtonian creep case ($n > 1$) exhibits qualitatively the same manner
187 (see Supplementary discussion A). We will see next that the prefactors or the maximum
188 amounts of the slip and slip rate, denoted by $\max u$ and $\max \dot{u}$, essentially involve the
189 temperature effect collectively.
190
191   **2.4 Temperature-dependent rheology**
192   We incorporate the ambient temperature dependencies in the above strength
193 parameters. First, plastic flows are considered to describe ductility. The rock viscosity η
194 is generally described by the Arrhenius-type temperature dependence [*Karato*, 2008]
195        $\eta(T) = \eta_o \exp(H/RT) \sim \eta_o \exp(gT_m/T)$ (2)
196 with the absolute temperature T, the activation enthalpy H, the gas constant R, the
197 melting temperature T_m and a constant η_o. The detailed dependence of η_o on the grain
198 sizes and the fugacity [*Karato*, 2008] are irrelevant to the qualitative behavior of the
199 system and are discarded in the current analysis. The pressure (P) dependence of the
200 viscosity is much weaker than that of temperature and is indirectly considered in the
201 model through the pressure dependence of $H(P)$ and $T_m(P)$[*Karato*, 2008]. Experiments
202 show that the constant g is of the order of ten[*Karato*, 2008; *Rutter and Brodie*, 2004],
203 and T_m is related to the onset temperature of plasticity as $T_m = g'T_p$ with g' being
204 severalfold for rocks [*Scholz*, 2019].
205   The temperature dependence of the brittle fraction $R_b(T)$ can be constrained by
206 the geodetic estimate of the interpolate coupling coefficient, which is determined by the
207 area of the locked (i.e., brittle) patches over the otherwise steady sliding areas. Geodetic

observations generally show that the coupling coefficients gradually decrease and moderately change with increasing depth or temperature, as illustrated in Figure 1a [*Avouac*, 2015; *Burgmann*, 2018]. Seismological observations also show a similar tendency for rupture areas to become smaller for deeper earthquakes [*Lay et al.*, 2012]. To model these gradual changes generically, we take a simple approach, assuming several types of functional forms (Figure 4a) and test the robustness of the outcome; such functions should satisfy the condition of the abovementioned monotonic decrease within the transition zone from $R_b(T_{fb}) = 1$ to $R_b(T_{fp}) = 0$ for $T_{fb} < T < T_{fp}$, where T_{fb} and T_{fp} respectively indicate the temperatures at the base of the fully brittle seismogenic zone and the top of the fully plastic aseismic zone. Typical examples of such functions may be given by

$$R_b(T) = \begin{cases} 1 - \{(T - T_{fb})/(T_{fp} - T_{fb})\}^c & for \ T_{fb} < T < T_{fp} \\ Step(T), \end{cases} \qquad (3)$$

where c is a constant and $Step(T)$ is a multi-step function plotted in Figure 4a. The multi-step function is hypothesized to mimic sudden changes due to some phase transitions.

2.5 Connecting temperature-dependent rheology with mechanical model parameters

The effects of the ambient temperature T are considered time-independent and are included in the above "macroscopic" strength parameters: $f_s(T) - f_d(T)$ and $\alpha(T)$. We introduce a constant for the force drop, Δf_o, corresponding to the value to be attained at the fully brittle case ($R_b = 1$). Similarly, for the ductile strength when fully ductile, we introduce the velocity-strengthening ratio $\alpha_o(T)(\equiv \eta(T) \times D/w$ with the fault dimension D and fault zone width w.) We do not explicitly concern about the effect of the fault zone width w increasing as going deeper [*Scholz*, 2019] because this effect is merely further decrease η_v together with the temperature dependent decrease of η. In analogy with the real contact area, these parameters constitute the macroscopic strength parameters with the brittle fraction $R_b(T)$ as the function of temperature in the brittle-ductile transitional regime, given by

$$f_s(T) - f_d(T) = R_b(T)\Delta f_o$$

for the brittle strength and, representing the otherwise ductile area,

$$\alpha(T) = [1 - R_b(T)]\alpha_o(T)$$

for the ductile strength, as illustrated in Figures 1c and 3a.

3 Results

243

3.1 General temperature dependence of slip modes

We are interested in the final slip $\max u$ and the maximum slip rate $\max \dot{u}$ during a single slip event occurring under the ambient temperature T. By considering the above-described temperature-dependent parameters and the temperature-independent rigidity k, it is given by

$$\max u(T) \propto f_s(T) - f_d(T) = \Delta f_o\left[1 - \left\{(T - T_{fb})/(T_p - T_{fb})\right\}^c\right] \qquad (4)$$

and

$$\max \dot{u}(T) \propto \frac{f_s(T) - f_d(T)}{\alpha(T)} = \frac{\Delta f_o\left[1 - \left\{(T - T_{fb})/(T_p - T_{fb})\right\}^c\right]}{\eta_o\left\{(T - T_{fb})/(T_p - T_{fb})\right\}^c \exp(gT_m/T)}. \qquad (5)$$

Figure 4b plots the viscosity for the dashpot as the function of temperature, exhibiting the extremely rapid reduction attributed to the Arrhenius law. Figure 4c shows the obtained temperature dependence of the force drop or final slip amount (Equation 4). The force drop and slip are merely proportional to $R_b(T)$ because the temperature dependence only appears through the brittle fraction $R_b(T)$. The force drop and slip are decreased as the function of temperature toward T_{fp} as intuitively understood.

3.2 SIL: Seismogenic peak at an intermediate temperature in the deep transition zone

Figure 4d shows the slip rate (Equation 5), which becomes influenced by the temperature dependence of η via α. The remarkable feature presented here is that the prominent peak appears at an intermediate temperature. This peak of the slip rate may not be intuitive. However, this simply manifests the decreasing viscosity as increasing temperature because the smaller viscous resistance leads to faster slip. The brittle fraction $R_b(T)$ and slip tend to decrease as well, but their decrease is much gentler and bounded $0 < R_b(T) < 1$. Such a gentle temperature dependence is easily overcome by the more rapid reduction of the viscosity due to the Arrhenius-type dependence, $\exp(1/T)$ (Figure 4b). (This mechanism is also the reason for a subtle peak at a lower temperature in the multi-step function case because the greater viscosity damps the motion at the first peak.) In other words, such a peak or SIL should exist as long as the viscosity is described by rapidly changing functions like the Arrhenius law.

It is further shown in Figure 4d that the existence of the peak at the intermediate temperature $\left(T_{fb} < T < T_{fp}\right)$ is independent of the assumed functional form of $R_b(T)$.

275   Further, if $c = 1$ in Equation 3, the peak slip rate always appears at the intermediate
276   temperature T_{sr} given by

277
$$T_{sr} = \left\{ (T_{fb} + T_p)/2 + \sqrt{(T_p - T_{fb})^2/4 - T_p^2 T_{fb}/gT_m} \right\}/(1 + T_p/gT_m) \quad (6)$$

278   with the inequality $T_{fb} < T_{sr} < T_p < gT_m$ (detailed in Supplementary material C). This
279   equation predicts that T_{sr} appears somewhat below the temperature of full plasticity, T_{fp}.
280   Additionally, across the trough from the peak, the slip rate in Figure 4d tends to exhibit a
281   rapid increase as the temperature decreases down to the base of the seismogenic zone,
282   T_{fb}, since the ductile strength is to vanish there.
283
284

285   **4. Discussions**
286   **4.1 Comparison with geophysical observations of deep slow earthquakes**
287   Our analysis results demonstrate that the stress drop (force drop divided by fault
288   area) and the slip decrease with increasing temperature or depth, coinciding with the
289   observed characteristics (Figure 1a). Furthermore, under the constant loading rate, the
290   frequency of events also becomes higher as increasing depth due to the smaller stress drop
291   there. These features can naturally explain the observed small stress drop of the slow
292   earthquakes [*Ide et al.*, 2007; *Miyazaki et al.*, 2006] together with the relatively larger
293   stress drop and longer intervals of L-SSEs than those of S-SSEs [*Frank et al.*, 2015;
294   *Hirose and Obara*, 2005; *Miyazaki et al.*, 2006] (Figure 1). Further, the simulated velocity
295   reproduces the observed peak at an intermediate temperature or depth seen as SIL.
296   Besides, the sliding event could appear steady for the lower temperature side due to the
297   smaller slip rate caused by larger viscosity; this situation perhaps explains the absence of
298   or unfound L-SSEs in Cascadia or San Andreas.
299

300   **4.2 Implications for rheological mechanisms of shallow-slow earthquakes**
301   Slow earthquakes are also observed in a shallow transition zone above the
302   seismogenic zone [*Ito and Obara*, 2006; *Obara*, 2011; *Obara et al.*, 2010]. While their
303   depth dependences are yet to be established, SIL has not been found even in one of the
304   best-observed subduction zone, Nankai trough, with ocean-bottom sensors thus far [*Araki
305   et al.*, 2017; *Nakano et al.*, 2018]. It may be worth discussing the implication of the current
306   model. The velocity-strengthening friction of clays is proposed to underlie shallow-slow
307   earthquakes [*Saffer and Marone*, 2003] through positive values of the nominal velocity
308   sensitivity factor $A \equiv (a - b)\sigma_n$, where $(a - b)$ and σ_n denote the rate- and state-

309   dependent frictional parameter and the effective normal stress. Based on the laboratory
310   experiments at a low-temperature regime, they infer A to be a weakly decreasing function
311   or independent of the depth toward the top of the fully-brittle depth D_{fb}, as simply
312   represented by the red and blue lines in Figure 4f, respectively, without loss of generality.
313   To explore the mechanism of the shallow events, we assume the depth-
314   dependence similarly to the temperature-dependence of the deep ones but incorporate the
315   abovementioned depth-dependence of the rate-dependent friction at a low-temperature
316   regime (detailed in Supplementary method D). The depth D dependence of the
317   parameters A and R_b are taken in general power-law forms respectively as a decreasing

318   function $A(D) = A_o\left\{1 - \left(D/D_{fb}\right)^{c_1}\right\}$ with constants $A_o > 0$ and $c_1 \geq 0$ (Figure 4f) and

319   as an increasing function $R_b(D) = \left(D/D_{fb}\right)^{c_2}$ with a constant $c_2 > 0$ (Figure 4e).

320   Following the same algebra, we obtained the expressions as $\max u(D) \propto \Delta f\left(D/\right.$

321    $\left.D_{fb}\right)^{c_2}$ and $\max \dot{u}(D) \propto \Delta f_o\left(D/D_{fb}\right)^{c_2}/\left[A_o\left\{1 - \left(D/D_{fb}\right)^{c_2}\right\}\left\{1 - \left(D/D_{fb}\right)^{c_1}\right\}\right]$. As

322   exemplified for $c_1 = 0\ and\ 1$ with $c_2 = 1$ (Figure 4i-h), the calculated slip rate is
323   increased monotonically up to the fully brittle depth (Figure 4h). This trend is simply
324   because the brittle fraction increases while the ductile strength vanishes with increasing
325   depth. This result seems to match the observation of the absence of SIL for the shallow
326   transition zone.
327

4.3 Implications for physics-based models of deep-slow earthquakes

329   The temperature dependence of the velocity-strengthening friction further
330   contributes to identifying the origin of the ductility controlling slow earthquakes in the
331   deep transition zone. In a high-temperature regime, laboratory experiments [*Blanpied et*
332   *al.*, 1995; *den Hartog et al.*, 2012; *Okamoto et al.*, 2019] show that the velocity-
333   strengthening friction tends to increase the sensitivity to the velocity with increasing
334   temperature, as shown in Figure 1b and simplified in Figure 4j (blue line). The
335   consequence of this tendency, along with the reduction of R_b (Figure 4i), gives the
336   symmetric patterns with the shallow case (Figure 4e-h), obtained simply by flipping and
337   replacing D with T. The setup of $(a - b)$ in the blue line case (Figure 4f and j) is
338   qualitatively the same as those of the common in the rate- and state-dependent fault
339   models for both the shallow and deep sides [e.g., *Tse and Rice*, 1986]. As a result, the slip
340   amount shows the monotonic decrease as increasing temperature (Figure 4k), similarly to
341   the plasticity case (Figure 4c). We further observe the monotonic decrease of the slip rate

as increasing temperature without exhibiting SIL (Figure 4l). The latter clearly shows the different outcomes from the current knowledge in the temperature dependences of the plastic creep and the rate-dependent friction.

Regarding the reproducibility of SIL, we preferer the deep-slow earthquake models with the plastic flow mechanisms together with brittle-ductile heterogeneities [e.g., *Ando et al.*, 2012; *Beall et al.*, 2019] rather than any models incorporating the rate-dependence of friction. The application of the rate- and state-dependent friction should work in determining the base of the seismogenic zone due to the overall velocity-weakening to strengthening transition [e.g., *Noda and Shimamoto*, 2012; *Scholz*, 2019]. However, this application in the macroscopic viewpoint (that homogenizes the rock heterogeneity) predicts a monotonic change from the fully seismic (fast slip) to aseismic regimes along the depth via the slow slip regime associated with the neutral stability mechanism [e.g., *Liu and Rice*, 2007]. Thus, the physics-based models in this line of thinking will be insufficient to explain the presence of SIL. Additional microscopic factors will be needed, which naturally arise from the internal heterogeneity of fault rock rheology emerging at the transitional P-T condition.

5 Conclusion

We develop a simple physics-based model of slow earthquakes that incorporates the temperature dependence of rock rheology in the brittle-ductile transitional regime. Geological observations of the plastically-deformed matrix and competent blocks in mineralogically heterogeneous fault zones are mimicked. Our model naturally reproduces the seismogenic inversion layer (SIL) without finely tuning rheological parameters. The key mechanism is the reduction in both the fraction of brittle blocks and the viscosity of the matrix with increasing temperature/depth independent of tectonic settings.

Open research

378   Data is available through Ujiie et al., 2022 and Tulley et al., 2022.
379

380   **Author contributions**
381   R. A. designed the project, developed the mechanical model, conducted the analysis and
382   wrote the manuscript. K. U., N. N. and Y. M. conducted the field survey and developed
383   the geological interpretations. All authors discuss the results and contribute to the writing.
384

385   **Competing interest statement**
386   The authors declare no competing interests.
387

388

389   **References**
390

391   Ando, R., N. Takeda, and T. Yamashita (2012), Propagation dynamics of seismic and aseismic
392   slip governed by fault heterogeneity and Newtonian rheology, *J. Geophys. Res.*, *117*, B11308,
393   doi:10.1029/2012jb009532.
394   Araki, E., D. M. Saffer, A. J. Kopf, L. M. Wallace, T. Kimura, Y. Machida, S. Ide, E. Davis,
395   and E. S. Scientist (2017), Recurring and triggered slow-slip events near the trench at the
396   Nankai Trough subduction megathrust, *Science*, *356*(6343), 1157-1160,
397   doi:10.1126/science.aan3120.
398   Audet, P., M. G. Bostock, N. I. Christensen, and S. M. Peacock (2009), Seismic evidence for
399   overpressured subducted oceanic crust and megathrust fault sealing, *Nature*, *457*(7225), 76-
400   78.
401   Avouac, J. P. (2015), From Geodetic Imaging of Seismic and Aseismic Fault Slip to Dynamic
402   Modeling of the Seismic Cycle, *Annual Review of Earth and Planetary Sciences, Vol 43*, *43*,
403   233-271, doi:10.1146/annurev-earth-060614-105302.
404   Beall, A., A. Fagereng, and S. Ellis (2019), Fracture and Weakening of Jammed Subduction
405   Shear Zones, Leading to the Generation of Slow Slip Events, *Geochem. Geophys. Geosyst.*,
406   *20*(11), 4869-4884, doi:10.1029/2019gc008481.
407   Behr, W. M., A. J. Kotowski, and K. T. Ashley (2018), Dehydration-induced rheological
408   heterogeneity and the deep tremor source in warm subduction zones, *Geology*, *46*(5), 475-478,
409   doi:10.1130/G40105.1.
410   Blanpied, M. L., D. A. Lockner, and J. D. Byerlee (1995), Frictional Slip of Granite at
411   Hydrothermal Conditions, *J. Geophys. Res.*, *100*(B7), 13045-13064, doi:Doi
412   10.1029/95jb00862.
413   Bos, B., and C. J. Spiers (2002), Frictional-viscous flow of phyllosilicate-bearing fault rock:

414 Microphysical model and implications for crustal strength profiles, *J. Geophys. Res.*, *107*(B2),

415 doi:10.1029/2001jb000301.

416 Boyer, F., E. Guazzelli, and O. Pouliquen (2011), Unifying Suspension and Granular Rheology,

417 *Phys. Rev. Lett.*, *107*(18), doi:10.1103/PhysRevLett.107.188301.

418 Burgmann, R. (2018), The geophysics, geology and mechanics of slow fault slip, *Earth Planet*

419 *Sc Lett*, *495*, 112-134, doi:10.1016/j.epsl.2018.04.062.

420 Currie, C. A., R. D. Hyndman, K. Wang, and V. Kostoglodov (2002), Thermal models of the

421 Mexico subduction zone: Implications for the megathrust seismogenic zone, *J. Geophys. Res.*,

422 *107*(B12), doi:10.1029/2001jb000886.

423 Daub, E. G., D. R. Shelly, R. A. Guyer, and P. A. Johnson (2011), Brittle and ductile friction

424 and the physics of tectonic tremor, *Geophys. Res. Lett.*, *38*, L10301,

425 doi:10.1029/2011GL046866.

426 den Hartog, S. A. M., A. R. Niemeijer, and C. J. Spiers (2012), New constraints on megathrust

427 slip stability under subduction zone P-T conditions, *Earth Planet Sc Lett*, *353*, 240-252,

428 doi:10.1016/j.epsl.2012.08.022.

429 Fagereng, A., G. W. B. Hillary, and J. F. A. Diener (2014), Brittle-viscous deformation, slow

430 slip, and tremor, *Geophys. Res. Lett.*, *41*(12), 4159-4167.

431 Frank, W. B., M. Radiguet, B. Rousset, N. M. Shapiro, A. L. Husker, V. Kostoglodov, N. Cotte,

432 and M. Campillo (2015), Uncovering the geodetic signature of silent slip through repeating

433 earthquakes, *Geophys. Res. Lett.*, *42*(8), 2774-2779, doi:10.1002/2015gl063685.

434 Hacker, B. R., G. A. Abers, and S. M. Peacock (2003), Subduction factory - 1. Theoretical

435 mineralogy, densities, seismic wave speeds, and H2O contents, *J. Geophys. Res.*, *108*(B1),

436 doi:10.1029/2001JB001127.

437 Hirose, H., and K. Obara (2005), Repeating short- and long-term slow slip events with deep

438 tremor activity around the Bungo channel region, southwest Japan, *Earth Planets Space*,

439 *57*(10), 961-972.

440 Howell, D., R. P. Behringer, and C. Veje (1999), Stress fluctuations in a 2D granular Couette

441 experiment: A continuous transition, *Phys. Rev. Lett.*, *82*(26), 5241-5244,

442 doi:10.1103/PhysRevLett.82.5241.

443 Hyndman, R. D., P. A. McCrory, A. Wech, H. Kao, and J. Ague (2015), Cascadia subducting

444 plate fluids channelled to fore-arc mantle corner: ETS and silica deposition, *J. Geophys. Res.*,

445 *120*(6), 4344-4358, doi:10.1002/2015jb011920.

446 Ide, S., G. C. Beroza, D. R. Shelly, and T. Uchide (2007), A scaling law for slow earthquakes,

447 *Nature*, *447*(7140), 76-79.

448 Ito, Y., and K. Obara (2006), Very low frequency earthquakes within accretionary prisms are

449 very low stress-drop earthquakes, *Geophys. Res. Lett.*, *33*(9), doi:10.1029/2006gl025883.

450   Karato, S. I. (2008), Deformation of Earth Materials: An Introduction to the Rheology of Solid

451   Earth, *Deformation of Earth Materials: An Introduction to the Rheology of Solid Earth*, 1-

452   463, doi:10.1017/Cbo9780511804892.

453   Katayama, I., T. Terada, K. Okazaki, and A. Tanikawa (2012), Episodic tremor and slow slip

454   potentially linked to permeability contrasts at the Moho, *Nat Geosci*, *5*(10), 731-734,

455   doi:10.1038/Ngeo1559.

456   Kobayashi, A. (2017), Objective detection of long-term slow slip events along the Nankai

457   Trough using GNSS data (1996-2016), *Earth Planets Space*, *69*, doi:10.1186/s40623-017-

458   0755-7.

459   Lay, T., H. Kanamori, C. J. Ammon, K. D. Koper, A. R. Hutko, L. L. Ye, H. Yue, and T. M.

460   Rushing (2012), Depth-varying rupture properties of subduction zone megathrust faults, *J.*

461   *Geophys. Res.*, *117*, doi:10.1029/2011JB009133.

462   Liu, Y. J., and J. R. Rice (2007), Spontaneous and triggered aseismic deformation transients

463   in a subduction fault model, *J. Geophys. Res.*, *112*(B9), B09404,

464   doi:doi:10.1029/2007JB004930.

465   Matsuzawa, T., B. Shibazaki, K. Obara, and H. Hirose (2013), Comprehensive model of short-

466   and long-term slow slip events in the Shikoku region of Japan, incorporating a realistic plate

467   configuration, *Geophys. Res. Lett.*, *40*(19), 5125-5130, doi:10.1002/grl.51006.

468   Michel, S., A. Gualandi, and J. P. Avouac (2019), Interseismic Coupling and Slow Slip Events

469   on the Cascadia Megathrust, *Pure Appl. Geophys.*, *176*(9), 3867-3891, doi:10.1007/s00024-

470   018-1991-x.

471   Miyazaki, S., P. Segall, J. J. McGuire, T. Kato, and Y. Hatanaka (2006), Spatial and temporal

472   evolution of stress and slip rate during the 2000 Tokai slow earthquake, *J. Geophys. Res.*,

473   *111*(B3), doi: 10.1029/2004JB003426

474   Mori, Y., M. Shigeno, and T. Nishiyama (2014), Fluid-metapelite interaction in an ultramafic

475   melange: implications for mass transfer along the slab-mantle interface in subduction zones,

476   *Earth Planets Space*, *66*, doi:10.1186/1880-5981-66-47.

477   Nakano, M., T. Hori, E. Araki, S. Kodaira, and S. Ide (2018), Shallow very-low-frequency

478   earthquakes accompany slow slip events in the Nankai subduction zone, *Nat Commun*, *9*,

479   doi:ARTN 984

480   10.1038/s41467-018-03431-5.

481   Nishiyama, T. (1989), Petrologic study of the Nagasaki metamorphic rocks in the Nishisonogi

482   peninsula–with special reference to the greenrock complex and the reaction-enhanced

483   ductility, *Mem. Geol. Soc. Japan*, *33*, 237-257.

484   Nishiyama, T. (1990), CO2-metasomatism of a metabasite block in a serpentine melange from

485   the Nishisonogi metamorphic rocks, southwest Japan, *Contributions to Mineralogy and*

486   *Petrology*, *104*(1), 35-46, doi:10.1007/BF00310644.

487   Noda, H., and T. Shimamoto (2012), Transient behavior and stability analyses of halite shear

488   zones with an empirical rate-and-state friction to flow law, *J. Struct. Geol.*, *38*, 234-242,

489   doi:10.1016/j.jsg.2011.08.012.

490   Obara, K. (2011), Characteristics and interactions between non-volcanic tremor and related

491   slow earthquakes in the Nankai subduction zone, southwest Japan, *J Geodyn*, *52*(3-4), 229-

492   248, doi:10.1016/j.jog.2011.04.002.

493   Obara, K., S. Tanaka, T. Maeda, and T. Matsuzawa (2010), Depth-dependent activity of non-

494   volcanic tremor in southwest Japan, *Geophys. Res. Lett.*, *37*, doi:10.1029/2010gl043679.

495   Okamoto, A. S., B. A. Verberne, A. R. Niemeijer, M. Takahashi, I. Shimizu, T. Ueda, and C. J.

496   Spiers (2019), Frictional Properties of Simulated Chlorite Gouge at Hydrothermal

497   Conditions: Implications for Subduction Megathrusts, *J. Geophys. Res.*, *124*(5), 4545-4565,

498   doi:10.1029/2018jb017205.

499   Peacock, S. M. (2009), Thermal and metamorphic environment of subduction zone episodic

500   tremor and slip, *J. Geophys. Res.*, *114*, B00A07, doi:doi: 10.1029/2008JB005978.

501   Rogers, G., and H. Dragert (2003), Episodic tremor and slip on the Cascadia subduction zone:

502   The chatter of silent slip, *Science*, *300*(5627), 1942-1943.

503   Rutter, E. H., and K. H. Brodie (2004), Experimental intracrystalline plastic flow in hot-

504   pressed synthetic quartzite prepared from Brazilian quartz crystals, *J. Struct. Geol.*, *26*(2),

505   259-270, doi:10.1016/S0191-8141(03)00096-8.

506   Saffer, D. M., and C. Marone (2003), Comparison of smectite- and illite-rich gouge frictional

507   properties: application to the updip limit of the seismogenic zone along subduction

508   megathrusts, *Earth Planet Sc Lett*, *215*(1-2), 219-235, doi:10.1016/S0012-821x(03)00424-2.

509   Scholz, C. H. (1998), Earthquakes and friction laws, *Nature*, *391*(6662), 37-42.

510   Scholz, C. H. (2019), *The Mechanics of Earthquakes and Faulting*, 3rd ed., Cambridge Univ.

511   Press, Cambridge, United Kingdom, doi:10.1017/9781316681473.

512   Segall, P., A. M. Rubin, A. M. Bradley, and J. R. Rice (2010), Dilatant strengthening as a

513   mechanism for slow slip events, *J. Geophys. Res.*, *115*, B12305, doi:10.1029/2010JB007449.

514   Shelly, D. R., and K. M. Johnson (2011), Tremor reveals stress shadowing, deep postseismic

515   creep, and depth-dependent slip recurrence on the lower-crustal San Andreas fault near

516   Parkfield, *Geophys. Res. Lett.*, *38*, doi:10.1029/2011gl047863.

517   Sibson, R. H. (1977), Fault rocks and fault mechanisms, *J. Geol. Soc. Lond.*, *133*(Part 3), 191-

518   213.

519   Skarbek, R. M., A. W. Rempel, and D. A. Schmidt (2012), Geologic heterogeneity can produce

520   aseismic slip transients, *Geophys. Res. Lett.*, *39*, doi:10.1029/2012gl053762.

521   Tse, S. T., and J. R. Rice (1986), Crustal Earthquake Instability in Relation to the Depth

522   Variation of Frictional Slip Properties, *J. Geophys. Res.*, *91*(B9), 9452-9472.

523   Tulley, C. J., A. Fagereng, K. Ujiie, J. F. A. Diener, and C. Harris (2022), Embrittlement

524   Within Viscous Shear Zones Across the Base of the Subduction Thrust Seismogenic Zone,

525   *Geochem. Geophys. Geosyst.*, *23*(9), doi:ARTN e2021GC010208

526   10.1029/2021GC010208.

527   Ujiie, K., K. Noro, N. Shigematsu, Å. Fagereng, N. Nishiyama, C. J. Tulley, H. Masuyama, Y.

528   Mori, and H. Kagi (2022), Megathrust Shear Modulated by Albite Metasomatism in

529   Subduction Mélanges, *Geochemistry, Geophysics, Geosystems*, *23*(8), e2022GC010569,

530   doi:https://doi.org/10.1029/2022GC010569.

531   Ujiie, K., H. Saishu, A. Fagereng, N. Nishiyama, M. Otsubo, H. Masuyama, and H. Kagi

532   (2018), An Explanation of Episodic Tremor and Slow Slip Constrained by Crack-Seal Veins

533   and Viscous Shear in Subduction Melange, *Geophys. Res. Lett.*, *45*(11), 5371-5379,

534   doi:10.1029/2018gl078374.

535   Wech, A. G., C. M. Boese, T. A. Stern, and J. Townend (2012), Tectonic tremor and deep slow

536   slip on the Alpine Fault, *Geophys. Res. Lett.*, *39*, doi:10.1029/2012gl051751.

537   Wech, A. G., K. C. Creager, and T. I. Melbourne (2009), Seismic and geodetic constraints on

538   Cascadia slow slip, *J. Geophys. Res.*, *114*, doi:10.1029/2008JB006090.

539   Zhu, L. P. (2000), Crustal structure across the San Andreas Fault, southern California from

540   teleseismic converted waves, *Earth Planet Sc Lett*, *179*(1), 183-190, doi:Doi 10.1016/S0012-

541   821x(00)00101-1.

542

543

544

Figures, table and captions

546

547 Table 1. Observation-based characterization of depth-dependent modes of
548 deep-slow earthquakes and host rock materials* from typical plate-interface
549 examples.

|	Subduction interfaces		Transform interfaces
	Nankai / Guerrero	Cascadia	San Andreas / Alpine
Shallow Cold	Regular earthquakes		
	Crust		
Shallower Colder	Long-term SSEs with no or little tremor [*Frank et al.*, 2015; *Kobayashi*, 2017]	No ETS found but not fully coupled [*Hyndman et al.*, 2015; *Michel et al.*, 2019]	No tremor found [*Shelly and Johnson*, 2011; *Wech et al.*, 2012]
	Crust	Crust	Crust
Deeper Warmer	Short-term SSEs with tremor or ETS [*Obara*, 2011]	SSEs with tremor (ETS). Shallower peak of Slip than that of tremor[*Wech et al.*, 2009]	Episodic tremor with possible episodic slip [*Shelly and Johnson*, 2011; *Wech et al.*, 2012]
	Mantle [*Obara*, 2011] / At Moho [*Currie et al.*, 2002]	Crust with unclear Moho [*Audet et al.*, 2009]	Crust [*Zhu*, 2000] / Mostly in lower crust [*Wech et al.*, 2012]
Deep Warm	Stable sliding		
	Mantle		

550 *Upper plate materials are indicated for subduction zones.

551

552

553

554
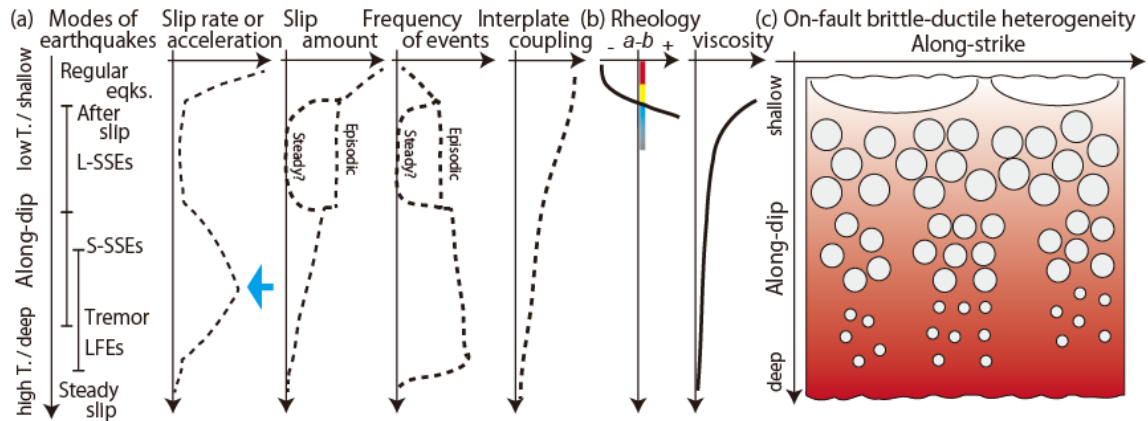
Figure1. Depth-dependent characteristics of deep slow earthquakes and fault rheology around the brittle-ductile transition depth. (a) Schematic diagrams of observed depth dependences of the parameters for individual slow earthquake events and the interplate coupling condition [*Avouac*, 2015; *Burgmann*, 2018]. The depth ranges and the modes of slow earthquakes are characterized as indicated; L-SSEs: Long-term slow slip events. S-SSEs: Short-term SSEs. LFEs: Low-frequency earthquakes. The blue arrow points to the peak in the seismogenic inversion layer (SIL). (b) Rheological properties on the slip velocity dependence coefficient $(a - b)$ of the rate- and state-friction (RSF) and the plastic flow viscosity. The colors along the vertical axis indicate the RSF regimes [*Scholz*, 1998] of unstable (red), conditionally stable (yellow), and stable (blue). (c) Schematics of the heterogeneous distribution of the rheological properties on a fault surface. The circles represent the brittle patches existing on the surrounding ductile background. The patch sizes/density and the background viscosity (indicated by the graded color) are decreasing functions of the depth.

569
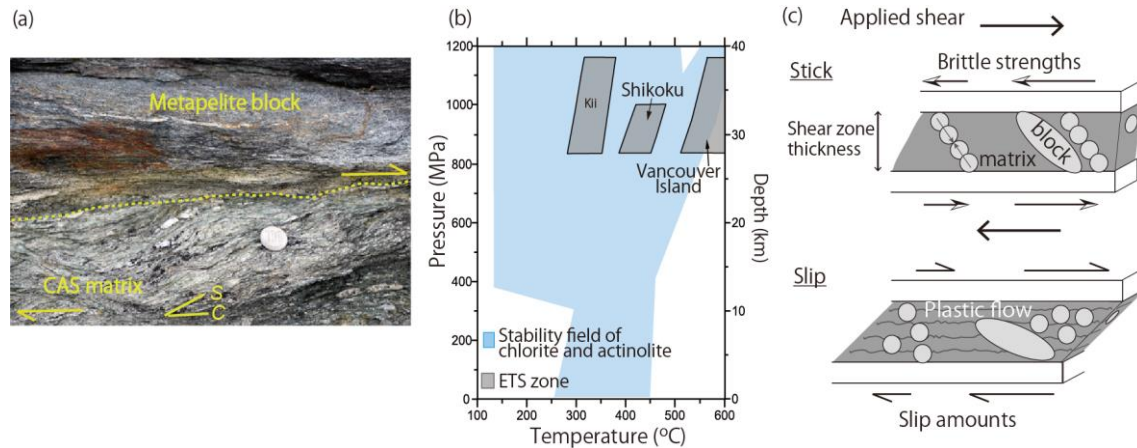
Figure 2. Internal material structure and deformation pattern of a fault zone. (a) Geologically observed block-in-matrix structure. Metapelite blocks surrounded by chlorite-actinolite schist (CAS) matrix. The arrows and lines respectively indicate the estimated shear sense and S-C fabrics. Outcrop examples in Nishikashiyama mélange, southwest Japan. (b) The P-T conditions for the stability field of chlorite and actinolite (redrawn from the facies of prehnite-actinolite, greenschist, epidote amphibolite, epidote-garnet amphibolite, lawsonite blueschist, jadeite lawsonite blueschist and epidote blueschist) [*Hacker et al.*, 2003] and the ETS zones in Nankai (Kii and Shikoku) and Cascadia (Vancouver island) subductions zones [*Peacock*, 2009]. (c) Schematics of fault zone motion. For the stick period (upper), the applied shear stress is resisted by the engaged brittle blocks with the stress chains. The denser distribution of blocks has a larger brittle strength. During a slip event (lower), the depinning due to the collapse and rotation of blocks release the shear stress slowly by the matrix plastic flows. The blocks are rearranged, forming force chains to be stuck again, recurring the stick-slip motion.
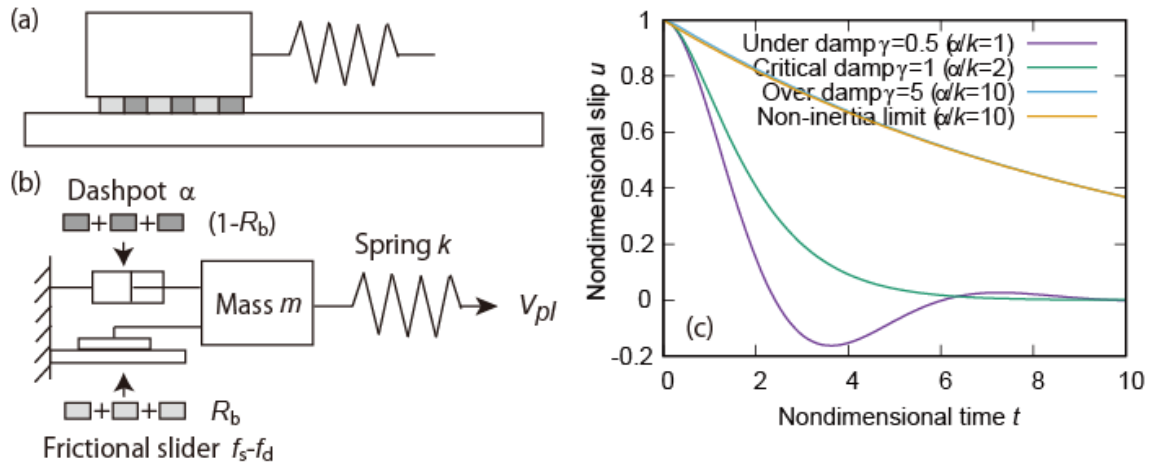
Figure 3. One degree of freedom model for a brittle-ductile heterogeneous fault. (a) The gross interfacial rheology determined by brittle areas with the brittle fraction R_b (light grey) and otherwise ductile areas (dark grey). (b) The modeling elements consisting of the dashpot and the slider, respectively representing the ductile and brittle sections in (a), which are connected in parallel to the mass and the spring. (c) Temporal progress of the block displacement (slip) for various values of the damping coefficient γ.

598

599
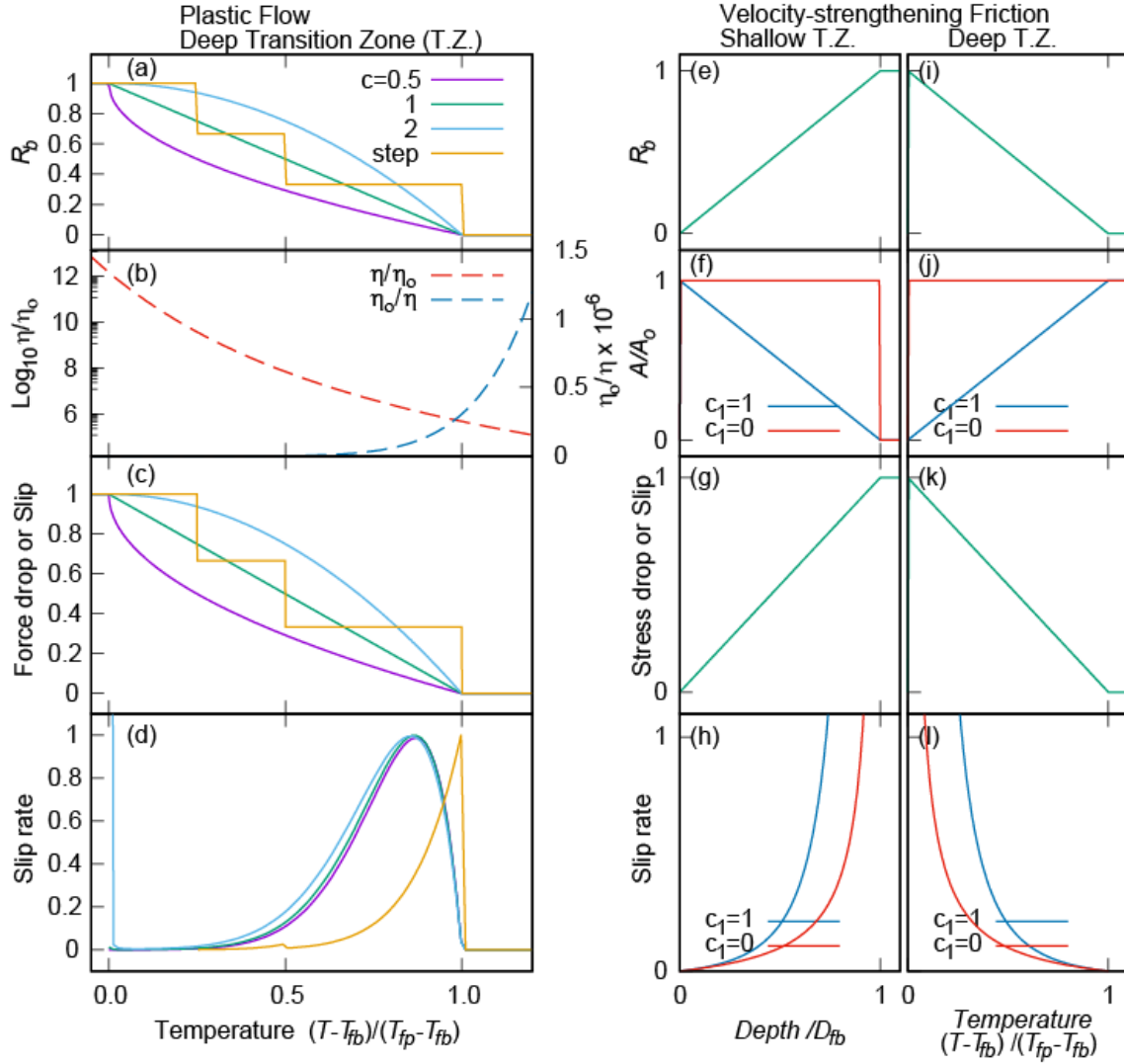
600 **Figure 4. Model conditions and simulated sliding characteristics as the function of**
601 **the temperature.** The horizontal axis, $T - T_{fb}$, indicates the temperature measured from
602 the base of the fully brittle zone (T_{fb}). (a)-(d) The case of plastic flow for the ductility of
603 the deep transition zone. (a) Assumed brittle fraction $R_b(T)$ for different dependences on
604 T as the power-low functions with the exponent $c = 0.5 - 2$ and the multi-step function.
605 (b) Normalized viscosity $\eta/\eta_o = \exp(gT_m/T)$ with $gT_m = 25(T_p - T_{fb})$. (c)
606 Normalized force drop and slip amount. (d) The maximum slip rate. The line colors in (a),
607 (c) and (d) indicate the cases of the same values of c. The cases of the simplified velocity-
608 strengthening friction applied to the shallow (e)-(h) and deep (i)-(l) transition zones. The
609 exponent c_1 discriminates the depth-dependence of the velocity strengthening ratio A (see
610 the main text for explanations). The values in the vertical axes are normalized by the
611 individual peak values in (c), (d), (g) and (k).